Validation of the hydrodynamics in a turbulent un-baffled vortex reactor at two different stirring Reynolds numbers

E. Saikali, G. Bois, M.G. Rodio, U. Bieder, A. Burlot, M. Bertrand

Version of Record: https://www.sciencedirect.com/science/article/pii/S0029549321004027
Manuscript_08dca774366621eb5ee4c7f3a0e0d6fb

Validation of the hydrodynamics in a turbulent un-baffled vortex reactor at two different stirring Reynolds numbers

E Saikali[†,*], G Bois[†], MG Rodio[†], U Bieder[†], A Burlot[†] and M Bertrand[‡]

[†] *Université Paris-Saclay, CEA, Service de Thermo-hydraulique et de Mécanique des Fluides, 91191, Gif-sur-Yvette, France,*
[‡] *CEA, Département de Recherche sur les Procédés pour la Mine et le Recyclage du Combustible, 30207, Bagnols-sur-Cèze, France,*
[*] *Corresponding author. E-mail address: elie.saikali@cea.fr*

Abstract

In this paper, a turbulent flow is simulated in an un-baffled stirred tank reactor with vortex effect by means of large eddy simulations. This work aims at validating the influence of increasing the stirring frequency on the hydrodynamics and compares the mixing regions that form in such configurations due to the presence of two main vortex types. The open source TRUST-TrioCFD code is used with a discontinuous front-tracking algorithm to capture the vortex that develops at the free surface. A rotating magnetic stirrer is modelled by an immersed boundary method with a penalization concept. Analysis of the auto-correlation function shows a different range of time micro-scales which depends on the spatial location and stirring frequency. A very good agreement is reported between the numerical solution and the experimental measurements and thus reflects the good quality of our numerical study. As far as no similar detailed work is reported in the literature, the numerical data is considered as a reference and will serve in a next step in modelling the formation of solid particles due to a precipitation process that takes place in many applications of energy and chemistry.

Keywords: Reactor with vortex effect (RVE); Large Eddy Simulation (LES); Discontinuous Front-Tracking (DFT); Auto-correlation; Energy spectrum; chemical reactors.

1. Context

In the domain of energy, whether in applications like battery recycling and radioactive waste processing, precipitations take place. Due to their chemical nature, these irreversible reactions are very fast and lead to the formation of solid crystal particles. As a consequence and for security reasons, it is extremely required to analyze and understand carefully the physical/chemical properties of the crystals formed. In order to provide the necessary knowledge regarding the properties of the crystals and to avoid waste manipulation at large scales, mixing tank reactors with a simplified design are often considered [1].

This study models an un-baffled tank where the fluid is agitated by a magnetic stirrer placed at the bottom of the reactor [2]. The choice of this design is done to avoid as much as possible the presence of accumulation/attrition zones that can build-up if a baffled reactor is considered. In addition, considering a magnetic stirrer instead of a mechanical one facilitate the maintenance procedures, waste management, and avoids the presence of major industrial issues that can reduce the efficiency of the process; blocking of the impeller for example.

The absence of the solid obstacles at the wall boundaries in an un-baffled tank makes the circular motion of the stirred fluid dominant over the other directions. Based on the mathematical Rankine's combined vortex model [3] and confirmed by the theoretical work of Nagata et al. [4], this rotational fluid orientation creates a vortex at the free surface which is similar to an inverted Gaussian profile. As a result, two macro-mixing zones characterizes the reactor. The first is located in the central region and described by a vertically-downward oriented vortex [5, 6]. It is known as the "forced vortex" where the fluid rotates as unified solid block with an angular velocity close to that of the stirrer. Otherwise, the flow is characterized by a helicoidal trajectory with an upward orientation that occupies about 96% of the reactor's volume. This defines the second mixing zone and is referred to by the "free vortex". Such behavior justifies why these configurations are cited as a reactor with a vortex effect (RVE).

The presence of the two mixing zones do not lead to a well mixed reactor and thus influences the precipitation process. For this reason, an accurate hydrodynamic modelling is required in order to reproduce the phenomenon. In this paper, a computational fluid dynamics (CFD) approach is followed as far as this tool has well shown to be efficient in accessing the local/global flow behavior when it is difficult experimentally. A large eddy simulations (LES) approach is chosen to model the strong anisotropic turbulence that builds in the RVE as far as performing a direct numerical simulation (DNS) is not possible. One of the main benefits of the LES approach is the possibility of accessing the fluctuating field which plays an important role in the study of precipitation and micro-mixing [7].

The objective of this study is to present and characterize the influence of the turbulence on the hydrodynamics in the RVE. Two different stirring Reynolds numbers are considered and validations are presented versus the available Laser Doppler Ve-

Nomenclature

RVE	Reactor with Vortex Effect	CFD	Computational Fluid Dynamics
DNS	Direct Numerical Simulations	LES	Large Eddy Simulations
SGS	Sub-Grid Scale	LDV	Laser Doppler Velocimetry
IBM	Immersed Boundary Method	DFT	Discontinuous Front Tracking
ACF	Auto Correlation Function	VEF	Finite Element Volume
$< \cdot >_t$	Time average operator	RMS$\{\cdot\}_t$	Root Mean Square operator
$*$	Superscript for dimensionless quantities		

C_W	WALE constant [-]	Re_s	Stirring Reynolds number [-]
t	Time variable [s]	δt	Time step [s]
H	Height of the reactor [m]	H_i	Height of the interface [m]
D	Length of the magnetic rod [m]	d	Diameter of the magnetic rod [m]
T	Diameter of the reactor [m]	Δ	Characteristic cell size [m]
$\mathbf{x} = (r, \theta, z)$	Space vector [m]	P	Pressure [Pa]
Ω^r	Resolved rotational strain tensor [s^{-1}]	$\mathcal{S}^r$	Resolved symmetrical strain tensor [s^{-1}]
N	Frequency of the rod's rotation [s^{-1}]	$\mathbf{u} = (u_1, u_2, u_3)$	Velocity field [$m.s^{-1}$]
σ	Surface tension [$N.m^{-1}$]	ρ	Density [$kg.m^{-3}$]
ν	Kinematic viscosity [$m^2.s^{-1}$]	$\mathcal{K}_{\mathrm{SGS}}$	Sub-Grid Scale kinetic energy [$m^2.s^{-2}$]
ν_{SGS}	Sub-Grid Scale viscosity [$m^2.s^{-1}$]	τ_{SGS}	Sub-Grid Scale stress tensor [$m^2.s^{-2}$]

locimetry (LDV) measurements of the experimental work carried out at CEA Grenoble. The document is organized as follows. In section two, the physical and the numerical modelling are presented. The numerical setup and the computational tools are discussed in section three. Instantaneous and statistical flow patterns are presented in section four. Section five is devoted to the turbulence analysis where the micro time frequencies are analyzed. Validations versus LDV measurements are the subject of section six. Concluding remarks and prospects are stated in section seven.

2. RVE modelling

2.1. Configuration

As introduced by [2] and without considering any inlet/outlet conditions, the simplified geometry of the reactor is described as a cylinder of height H and diameter T, with $H \approx 1.6T$. A free opening at the top is considered. The cylinder is filled with water at rest to a height $H_i < H$; density $\rho_{\mathrm{w}} = 1000\ \mathrm{kg.m^{-3}}$ and kinematic viscosity $\nu_{\mathrm{w}} = 1 \times 10^{-6}\ \mathrm{m^2.s^{-1}}$ of water are considered at room ambient conditions. As illustrated in figure 1, a flat free-surface separates water from air ($\rho_{\mathrm{a}} = 1.29\ \mathrm{kg.m^{-3}}$ and $\nu_{\mathrm{a}} = 2 \times 10^{-5}\ \mathrm{m^2.s^{-1}}$). A uniform/constant interfacial surface tension coefficient $\sigma = 0.07\ \mathrm{N.m^{-1}}$ is considered.

The magnetic rod has a length D and a diameter d, with $D/T \approx 0.47$ and $D/d \approx 6.7$. It is placed at the bottom-center of the cylinder to rotate in the clockwise direction and is thus the reason of the fluid motion. Two constant rotational frequencies N_1 and N_2 have been considered in this work leading to

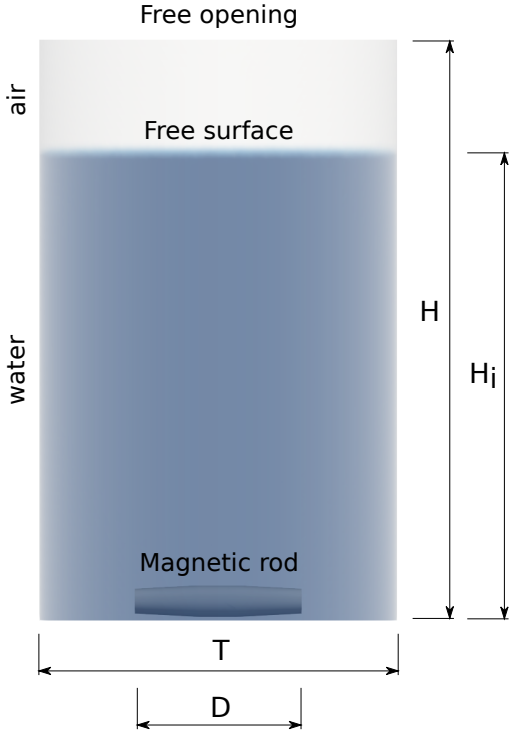

Figure 1: Schematic representation of the reactor's geometry.

two stirring Reynolds numbers: $\mathrm{Re}_{s_1} = N_1 D^2/\nu \approx 7 \times 10^4$ and $\mathrm{Re}_{s_2} = N_2 D^2/\nu \approx 8.6 \times 10^4$. In both cases, the flow is completely turbulent [8].

2.2. LES governing equations

Assuming an isothermal condition with no phase-change phenomenon, the flow is governed by the conservation equations of mass and momentum. Assuming no density variations flow with low Mach number (Ma $\approx 10^{-3}$), the incompressibility hypothesis of the fluid is valid. To simplify the reading of the document, the governing equations are presented for a single-fluid case. This formulation basically holds true far from the liquid/gas interface. However, the complete two-phase formulation is taken into account in the study where the surface tension and jumps are considered at the free surface. A detailed formulation for two-phase flows can be reviewed from [9, 10, 11].

Applying a spatial filter on the set of Navier-Stokes equations leads to the LES system of equations, written as

$$\nabla \cdot \overline{\mathbf{u}} = 0, \tag{1}$$

$$\frac{\partial \overline{\mathbf{u}}}{\partial t} + (\overline{\mathbf{u}} \cdot \nabla)\overline{\mathbf{u}} = -\frac{1}{\rho}\nabla \overline{P} + \nu \Delta \overline{\mathbf{u}} - \nabla \cdot \overline{\tau}^{\mathrm{SGS}} + \overline{\mathbf{F}}, \tag{2}$$

where the overbar symbol denotes the spatial filtering operator of the resolved scales. $\nabla, \nabla\cdot, \Delta$ denote the gradient, divergence and Laplacian operators respectively. ρ is the density, $\mathbf{u} = (u_1, u_2, u_3)$ is the velocity field, P the pressure and ν the kinematic viscosity. $\mathbf{F}$ denotes the sum of the external forces, like gravity $\mathbf{g} = (0, 0, -9.81)$ and surface tension force. $\overline{\tau}^{\mathrm{SGS}}$ is the sub-grid scale (SGS) stress tensor defined in terms of the tensorial product operation $\otimes$ as

$$\overline{\tau}^{\mathrm{SGS}} = \overline{\mathbf{u} \otimes \mathbf{u}} - \overline{\mathbf{u}} \otimes \overline{\mathbf{u}}. \tag{3}$$

The LES considered is implicit with respect to the mesh. This means that length scales smaller than the characteristic grid size Δ are modelled and their effects are attributed to the term $\overline{\tau}^{\mathrm{SGS}}$. The length scale Δ is locally considered as the cubic root of the cell volume.

In this paper, the wall-adapting local eddy-viscosity (WALE) model [12] is used as far as it is known to perform better than the classical model of Smagorinsky [13] especially near the solid boundaries, in shear layers and laminar-turbulent transitional phases. The WALE model is based on an eddy-viscosity assumption where the SGS-stress is expressed as

$$\overline{\tau}^{\mathrm{SGS}} - \frac{2}{3}\overline{\mathcal{K}}^{\mathrm{SGS}}\mathbb{I} = -2\nu^{\mathrm{SGS}}\mathcal{S}^r, \tag{4}$$

with $\mathbb{I}$ denoting the identity tensor and $\mathcal{S}^r$ the symmetrical part of the resolved (filtered) strain tensor, defined as

$$\mathcal{S}^r = \frac{1}{2}\Big[(\nabla \otimes \overline{\mathbf{u}}) + {}^t(\nabla \otimes \overline{\mathbf{u}})\Big]. \tag{5}$$

The SGS viscosity ν^{SGS} is thus calculated as

$$\nu^{\mathrm{SGS}} = (C_W \Delta)^2 \frac{(\mathcal{S}^d : \mathcal{S}^d)^{3/2}}{(\mathcal{S}^d : \mathcal{S}^d)^{5/4} + (\mathcal{S}^r : \mathcal{S}^r)^{5/2}}, \tag{6}$$

with the model parameter $C_W = 1/2$. ":" denotes the tensorial contraction operator. $\mathcal{S}^d$ is defined as

$$\mathcal{S}^d = \mathcal{S}^{r2} + \Omega^{r2} - \frac{1}{3}(\mathcal{S}^r : \mathcal{S}^r + \Omega^r : \Omega^r)\mathbb{I}, \tag{7}$$

where Ω^r denotes the rotational part of the resolved strain tensor, expressed as

$$\Omega^r = \frac{1}{2}\Big[(\nabla \otimes \overline{\mathbf{u}}) - {}^t(\nabla \otimes \overline{\mathbf{u}})\Big]. \tag{8}$$

Finally, the filtered SGS kinetic energy $\overline{\mathcal{K}}^{\mathrm{SGS}}$ that corresponds to the isotropic part of the SGS tensor is calculated with a Schumann's [14] approximation as

$$\overline{\mathcal{K}}^{\mathrm{SGS}} = \left(\frac{\nu^{\mathrm{SGS}}}{C_K \Delta}\right)^2, \tag{9}$$

with a constant $C_K = 0.094$.

To simplify the notations, the overbar symbol is removed in all what follows, keeping in mind that all presented quantities are the solved (filtered) ones.

3. Numerical Setup

3.1. Numerical methods

The numerical study is carried out by the CEA open source TrioCFD software within the TRUST platform [15, 16]. A numerical scheme combining finite volume and finite elements (VEF) is employed on tetrahedral cells to integrate in conservative form all conservation equations over the control volumes belonging to the calculation domain [17]. As in the classical Crouzeix–Raviart element, both vector and scalar quantities are located at the centers of the faces. The pressure, however, is located at the vertices and at the center of gravity of a tetrahedral element (see figure 2 for a 2D illustration). This discretization leads to very good pressure/velocity coupling and has a very dense divergence free basis [18]. Along this staggered mesh arrangement, the unknowns, i.e. the vector and scalar values, are expressed using non-conforming linear shape-functions (P1-nonconforming). The shape function for the pressure is constant for the center of the element (P0) and linear for the vertices (P1). In this study, the spatial discretization scheme is of second order for both convection and diffusion terms.

The time integration is explicit and the stability of the numerical scheme is ensured by respecting the Courant-Friedrichs-Lewy (CFL) condition as far as the flow is dominated by convection. A projection method is used to handle the velocity-pressure coupling, satisfying equation (1). The resulting pressure Poisson equation is solved with a conjugate gradient (CG) method with symmetrical-successive over relaxation (SSOR) preconditioning. A detailed presentation of the resolution algorithm can be reviewed from [19, 20].

An Immersed Boundary Method (IBM) is used with a Direct Forcing (DF) to model the stirrer motion [21]. The magnetic rod is defined as a moving Lagrangian mesh where a constant imposed speed is prescribed. The fluid/stirrer interaction is modelled by an additional penalization source term to the momentum equation (2). This method ensures that the real effect of the solid boundary exerted on the fluid is taken into account, based on its geometry, at each computational cell in the vicinity of the rod [22].

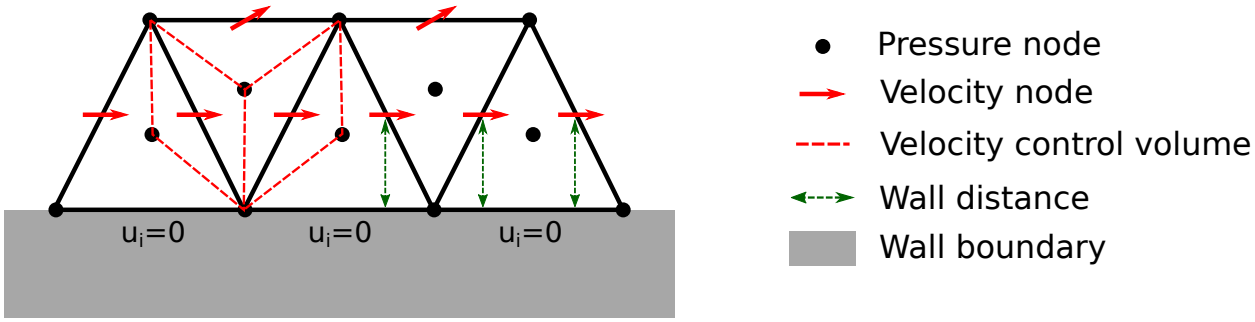

Figure 2: 2D illustration: arrangement of control volumes in a VEF discretization and determination of the wall distance.

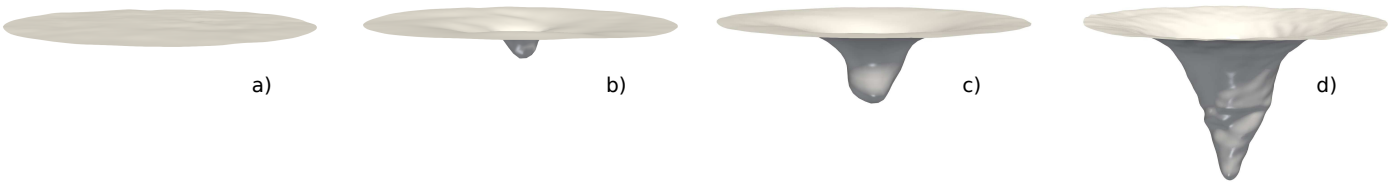

Figure 3: Free-surface deformation with time advancement. Simulation with $\mathrm{Re}_{s_1} \approx 7 \times 10^4$.

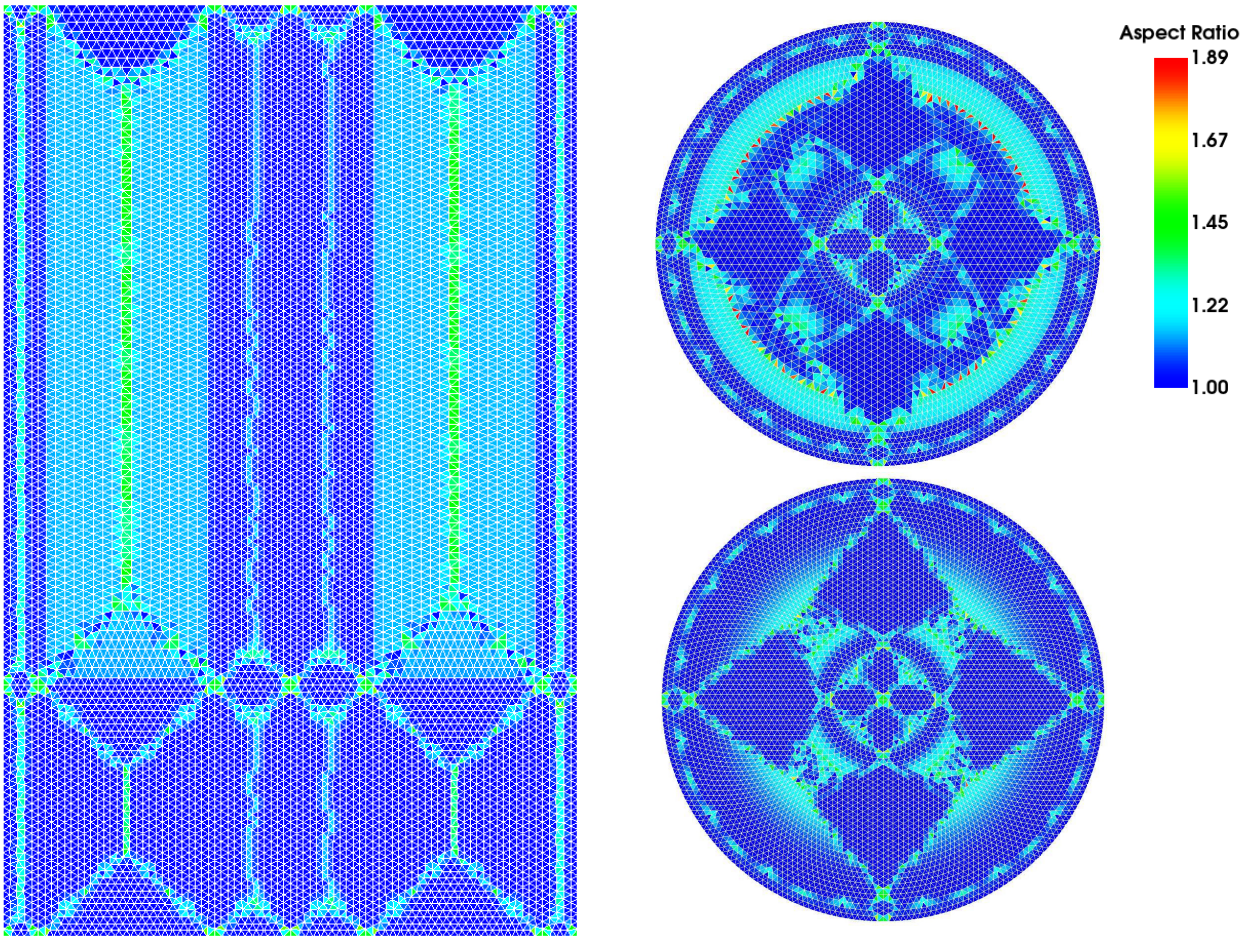

Figure 4: 2D aspect ratio q depicting the quality of the mesh taken from [6]. Left: 2D mid-vertical xz-plane, right-top: top open boundary, right-bottom: bottom wall boundary.

Due to the rotational motion of the stirrer, the free-surface separating the two-phases of the reactor deforms. The physical properties of each fluid are independently used, while velocity and pressure fields are considered simultaneously for both

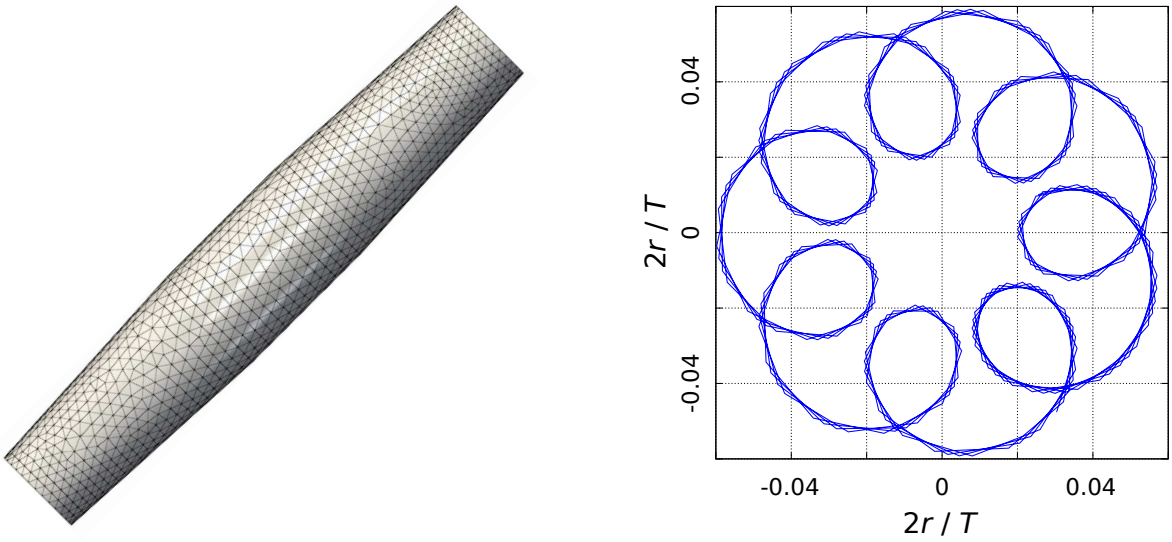

Figure 5: Left: the modelled magnetic stirrer depicting the employed Lagrangian moving mesh, right: the trajectory followed by the stirrer's center of gravity during the simulation in the horizontal $r\theta$-plane.

phases. To detect the free-surface deformation, a Discontinuous Front Tracking (DFT) method is employed. In the DFT algorithm, the free-surface is defined as moving connected-marker points (grid), independent of the employed Eulerian mesh. The moving Lagrangian grid is advected by a velocity field, which is interpolated from the solution to Navier-Stokes equations computed on the fixed Eulerian mesh. The new marker's positions are used to update the phase indicator function, and thus the physical properties of each phase; density and viscosity [11, 23, 24].

Figure 3 shows how the free-surface deforms with time, starting from a flat shape a), with a small tip in b), a bit larger in c) to take finally the well known Nagata profile in d).

3.2. Meshing, boundary conditions and wall law

The meshing is prepared with the open source SALOME platform [25]. A finer mesh is generated at the bottom, in the center and near the walls of the reactor. In the remaining part of the tank, a coarser mesh is considered. The mesh employed in this study is formed of about 3.4×10^6 tetras distributed over 112 MPI processors with $T/\Delta \approx 57 - 76$ (recall that T is the diameter of the reactor). Figure 4 shows the cells 2D aspect ratio q, defined in SALOME as

$$q = \frac{l_{\max} P}{4\sqrt{3}A}, \tag{10}$$

where A, P and $l_{\max}$ are respectively the area, perimeter and maximum edge of each triangle. The values of q reflect the good quality of the mesh when it is close to unity. The fine regions at the center and the bottom of the tank, in addition to the wall vicinity, are clearly noted.

As discussed in [6], the mesh size is of the same order as the Taylor turbulent micro-scale λ_T, estimated as

$$\lambda_T = \sqrt{\frac{10\,\nu\,\mathcal{K}_t}{\epsilon^{\mathrm{LES}}}}, \tag{11}$$

where $\mathcal{K}_t = 0.5\sum_{i=1}^{3} u_i' u_i'$ is the turbulent kinetic energy and $\epsilon^{\mathrm{LES}} = 2(\nu + \nu^{\mathrm{SGS}})(\mathcal{S}_{ij}^r \mathcal{S}_{ij}^r)$ the instantaneous total dissipation rate.

At the top free open boundary, Neumann conditions with an imposed pressure are prescribed. No-slip condition is defined on the wall boundaries where the contact angle of the free surface is kept perpendicular to them. A constant rotational law is prescribed for the magnetic stirrer in both simulations. Figure 5 (right) depicts the trajectory followed by the center of gravity of the stirrer which mimics the behavior observed in the real experiment. It is important to emphasize that wall functions are not considered in the present study for the stirrer boundary.

The standard Reichardt wall function is used to model the momentum exchange between walls and fluid and thus to improve the near wall flow resolution. This wall function spans, with one correlation, the three viscous, buffer and turbulent sublayers [26, 27]. The Reichardt formulation is expressed in terms of the non-dimensional wall distance y^+ and velocity U^+ as

$$U^+ = \frac{1}{0.415}\ln(1+0.415y^+) + 7.44\left(1 - e^{-y^+/11} - \frac{y^+}{11}e^{-y^+/3}\right). \tag{12}$$

In each phase of the reactor, the appropriate viscosity is used to calculate y^+. The viscosity values of the boundary cells laying in the vicinity of the interface are weighted by the indicator function which defines the position of the interface. For completeness, values recorded in this study ensure that the modelled layer lies in the logarithmic region, with $y^+ > 35$.

In the context of a VEF discretization and as illustrated in figure 2, the control volume of the velocity is built by connecting the associated pressure nodes. The distance of the near wall velocity to the wall can easily be determined as the distance of the center of gravity of the element's surface to the wall. If the meshing consists of tetrahedral meshes of similar sizes as shown in figure 2, the wall distance of all elements that have contact to the wall is very similar. This is also true for cells

with point contact. The described method has been used recently with success and is well detailed in [28, 29].

3.3. Dimensionless parameters and statistics

The dimensionless quantities presented in this document are all denoted by the * superscript. For the space variables, the dimensionless values are defined respectively as $r^* = 2r/T$ along the radial direction, $\theta^* = \theta/2\pi$ along the angular direction and $z^* = z/H$ along the axial direction. Following this notation, the space vector is denoted as $\mathbf{x} = (r, \theta, z)$.

As far as the geometry of the reactor is cylindrical, it is preferred to present the flow variables within a cylindrical coordinate reference frame. Thus, the radial component of the velocity field is defined as $u_r = u_1 \cos(\theta) + u_2 \sin(\theta)$, tangential as $u_\theta = u_2 \cos(\theta) - u_1 \sin(\theta)$ and axial as $u_z = u_3$. The dimensionless velocity components are defined as $u_i^* = u_i/u_{ref}$, where u_{ref} is the reference stirring velocity defined either as $\pi N_1 D$ or as $\pi N_2 D$. Finally, the dimensionless time is defined either as $t^* = N_1 t$ or $t^* = N_2 t$ and corresponds to the total number of complete rotations performed by the stirrer.

Numerical calculations have been carried out on the OCCIGEN – CINES cluster [30]. The time averaged and the root mean square (RMS) fields are defined as

$$< \varphi(\mathbf{x}, t) >_t = \frac{1}{t_{\text{end}} - t_{\text{start}}} \int_{t_{\text{start}}}^{t_{\text{end}}} \varphi(\mathbf{x}, t) dt, \tag{13}$$

$$\text{RMS}\{\varphi(\mathbf{x}, t)\}_t = \sqrt{\frac{1}{t_{\text{end}} - t_{\text{start}}} \int_{t_{\text{start}}}^{t_{\text{end}}} (\varphi'(\mathbf{x}, t))^2 dt}. \tag{14}$$

φ' denotes here the fluctuating part of a considered quantity φ, centered on the mean value, and defined as

$$\varphi'(\mathbf{x}, t) = \varphi(\mathbf{x}, t) - < \varphi(\mathbf{x}, t) >_t . \tag{15}$$

t_{start} denotes the starting time of the statistical recordings, while t_{end} corresponds to the end of the accumulation.

In order to accelerate the transient solution, the initial velocity field considered for both calculations is extrapolated from that obtained by a coarse LES having a well established turbulent flow. For the first simulation with a stirrer rotational frequency N_1, a quasi-steady state solution has been well established at $t^* \approx 25$. For the second simulation, it has been noted that the transient solution is slightly longer where the quasi-steady state solution is assumed to be reached at $t^* \approx 40$. Thus, the starting time of the statistical recording is fixed for both cases to $t^*_{\text{start}} = 50$. The simulated physical time is about $t^* \approx 150$, performed over about 30 days of CPU time in average. Numerical results and validations are presented in the remaining part of the document.

4. Hydrodynamics description

4.1. Instantaneous flow pattern

As stated previously, the flow in the RVE is characterized by two vortices, the forced and the free ones. As illustrated in figure 6, this behavior has been reported for both stirring Reynolds number. Here, the instantaneous iso-surfaces of the Q-criterion are presented at $t^* = 118$. The levels are colored according to the values of the vertical velocity u_z^* to illustrate on the flow orientation. In both cases, the central forced vortex is

Figure 6: Instantaneous iso-surfaces of the Q-criterion colored by the vertical velocity component u_z^* at $t^* = 118$. Left: $\text{Re}_{s_1} \approx 7 \times 10^4$, right: $\text{Re}_{s_2} \approx 8.6 \times 10^4$.

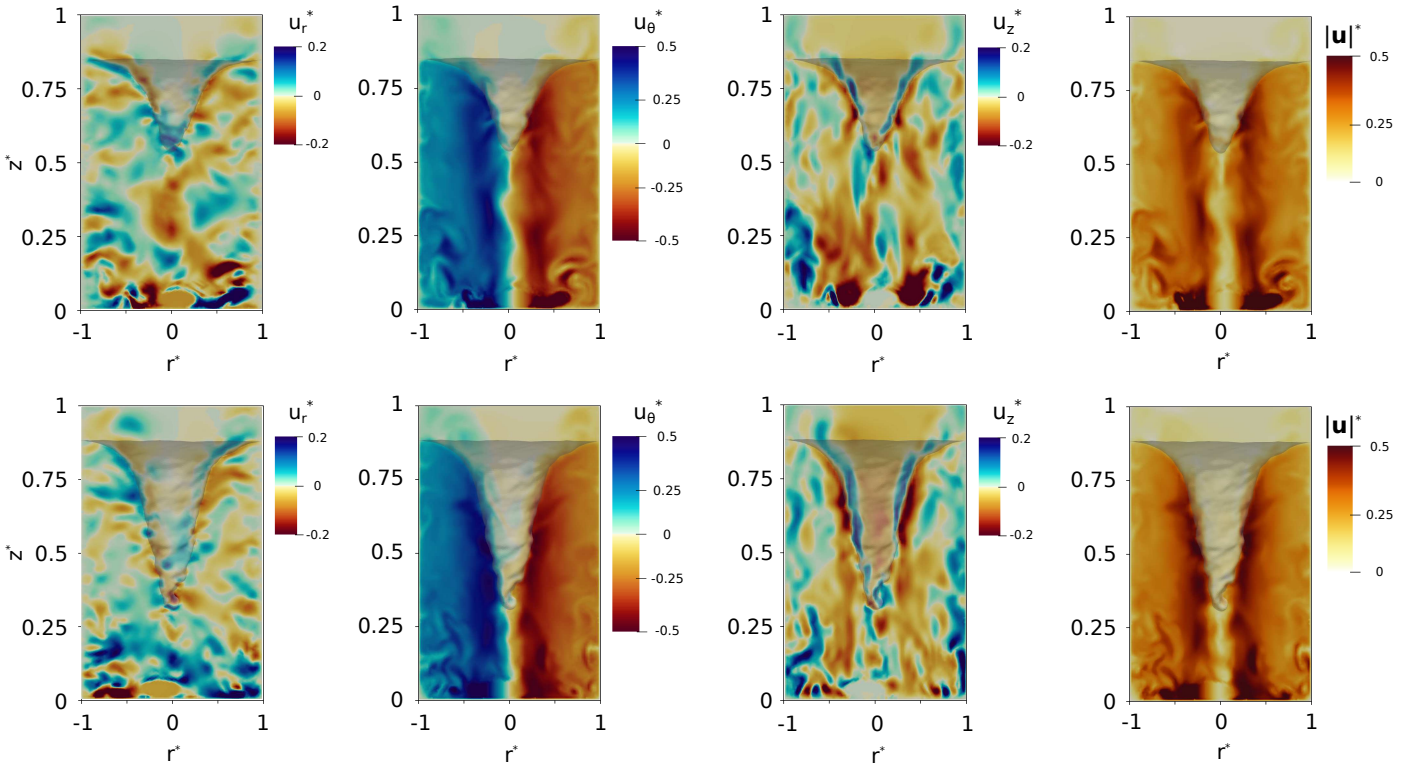

Figure 7: Instantaneous flow pattern illustrated by the velocity iso-contours at $t^* = 150$ in the mid-vertical rz-plane at $\theta^* = 0$. Left to right: radial velocity u_r^*, tangential velocity u_θ^*, axial velocity u_z^* and velocity magnitude $|\mathbf{u}|^*$ respectively. Top: $\mathrm{Re}_{s_1} \approx 7 \times 10^4$, bottom: $\mathrm{Re}_{s_2} \approx 8.6 \times 10^4$.

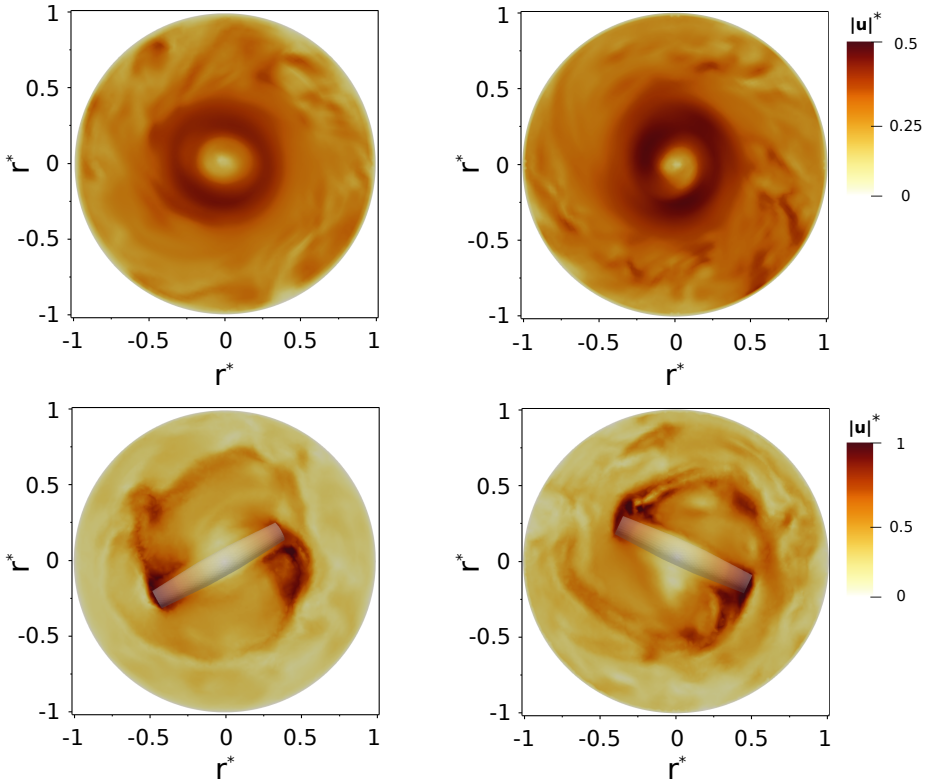

Figure 8: Instantaneous flow pattern illustrated by the dimensionless velocity magnitude $|\mathbf{u}|^*$ iso-contours at $t^* = 150$ in two horizontal planes. Bottom: $z^* = 0.03$, top: $z^* = 0.27$. Left: $\mathrm{Re}_{s_1} \approx 7 \times 10^4$, right: $\mathrm{Re}_{s_2} \approx 8.6 \times 10^4$.

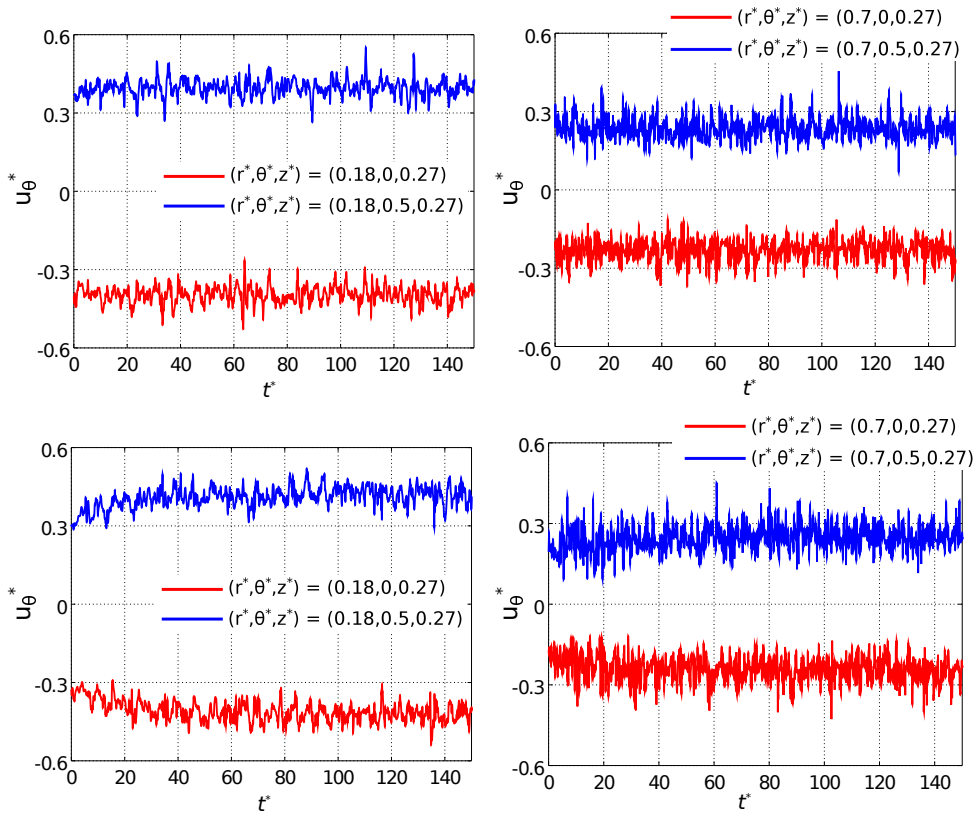

Figure 9: u^*_θ history profiles illustrating the unsteadiness and the fluctuating intensity in the RVE. Left: forced vortex region at $r^* = 0.18$, right: free vortex zone at $r^* = 0.7$. Top: $\mathrm{Re}_{s_1} \approx 7 \times 10^4$, bottom: $\mathrm{Re}_{s_2} \approx 8.6 \times 10^4$.

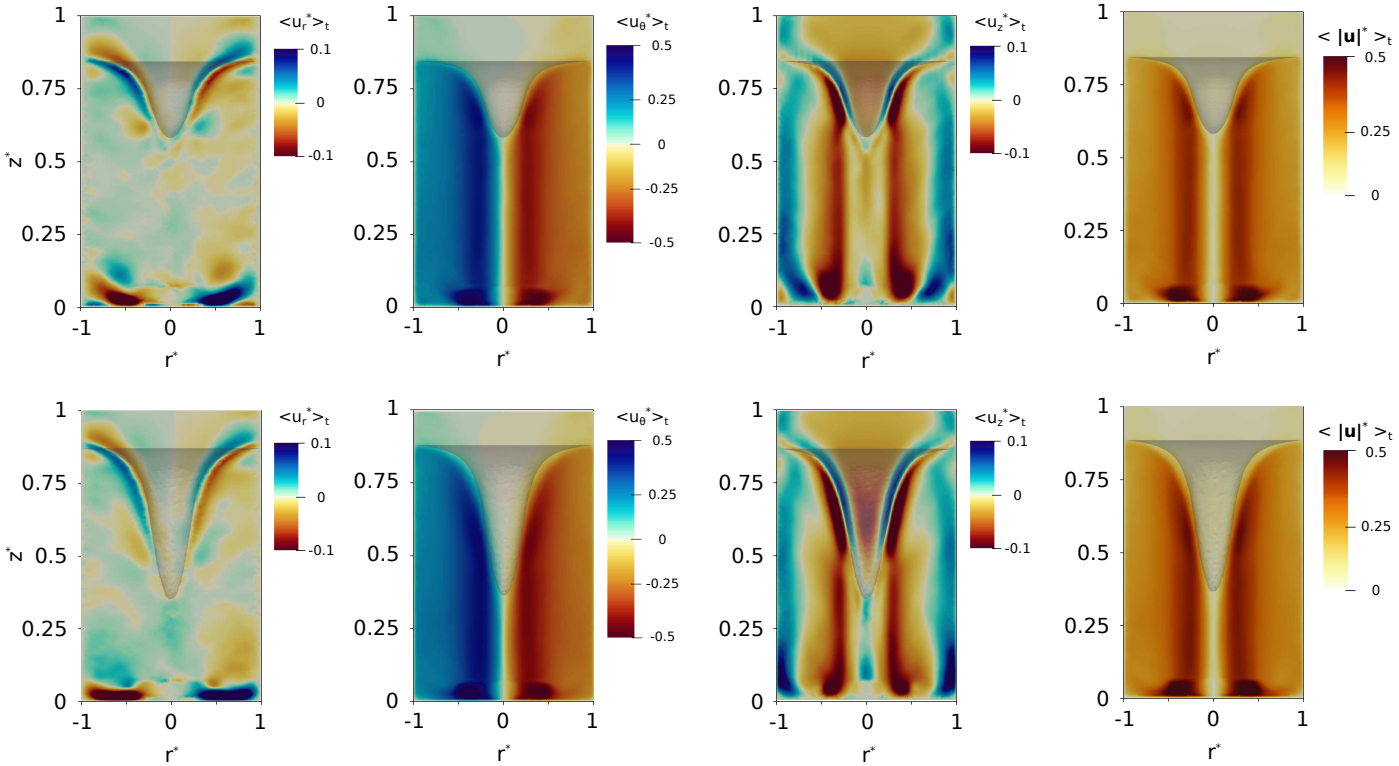

Figure 10: Time averaged flow pattern illustrated by the velocity iso-contours in the mid-vertical rz-plane at $\theta^* = 0$. Left to right: radial velocity $< u^*_r >_t$, tangential velocity $< u^*_\theta >_t$, axial velocity $< u^*_z >_t$ and velocity magnitude $< |\mathbf{u}|^* >_t$ respectively. Top: $\mathrm{Re}_{s_1} \approx 7 \times 10^4$, bottom: $\mathrm{Re}_{s_2} \approx 8.6 \times 10^4$.

oriented in the downward direction, while an upward direction is followed by the helicoidal free vortex. However, a qualitative influence is noted on the height of the free-surface vortex which is higher in the case of the larger stirring Reynolds number. The reader is kindly referred to [31] for additional comparisons regarding the free surface prediction and the size of the forced vortex with both stirring frequencies.

Next, the instantaneous flow pattern is presented in figure 7 at $t^* = 150$ where the iso-contours of all velocity components are depicted in the mid-vertical plane ($\theta^* = 0$). The figures at the top correspond to the first calculation ($\mathrm{Re}_{s_1} \approx 7 \times 10^4$), while those at the bottom are for the second one ($\mathrm{Re}_{s_2} \approx 8.6 \times 10^4$). In both cases, it can be easily noted that the flow is highly turbulent and that the tangential component u_θ dominates the other components. The interpretation of the radial u_r and the axial u_z iso-contours is not straight forward. However, it can be stated that their highest values are situated near the stirrer at the bottom of the tank and near the free-surface at the top.

To the contrary, the iso-contours of u^*_θ are easier to interpret where we note that the tangential distribution is almost symmetrical in both cases. Due to its dominance, the symmetrical observation can be furthermore confirmed by the velocity magnitude $|\mathbf{u}|^*$ iso-contours, either in the same vertical plane (figure 7), or in two horizontal planes situated at $z^* = 0.03$ and $z^* = 0.27$ (figure 8).

Moreover, in addition to the vicinity of the rod, the maximal u^*_θ values are predicted for both stirring frequencies around the central region of the reactor; the forced vortex zone. The values are reduced in the far field which corresponds to the zone of the free vortex, while they are almost null along the central axis of the reactor.

A quantitative illustration that concerns this observation is depicted in figure 9 where the time evolution of u^*_θ is considered at four pair-wise symmetrical probes. The probes are situated in the central forced region at $r^* = 0.18$ and in the free vortex region at $r^* = 0.7$, all at a height $z^* = 0.27$. The profiles hold a lot of information. Firstly, it is clear that the flow is completely unsteady in both cases. Moreover, the fluctuations intensity increases in the free vortex zone as illustrated for both calculations at $r^* = 0.7$, compared to those at $r^* = 0.18$. However, there is no significant influence on the intensity of the fluctuations by varying the Reynolds number.

Secondly, it is noted that the values of the tangential velocity decrease from the forced to free vortex zones. This observation is illustrated in both calculations and is well described by the Rankine's combined vortex model. Moreover, the dimensionless u^*_θ values confirm that the velocity of the fluid in the forced and in the free zones can be defined as a function of that of the stirrer.

4.2. *Statistical fields*

Figure 10 describes the time averaged flow pattern for both configurations. The iso-contours of all velocity components are presented in the mid vertical rz-plane at $\theta^* = 0$. The dominance of the rotational motion is confirmed again for both stirring frequencies. A good visible symmetrical distribution is noted on all velocity components. This can be furthermore confirmed

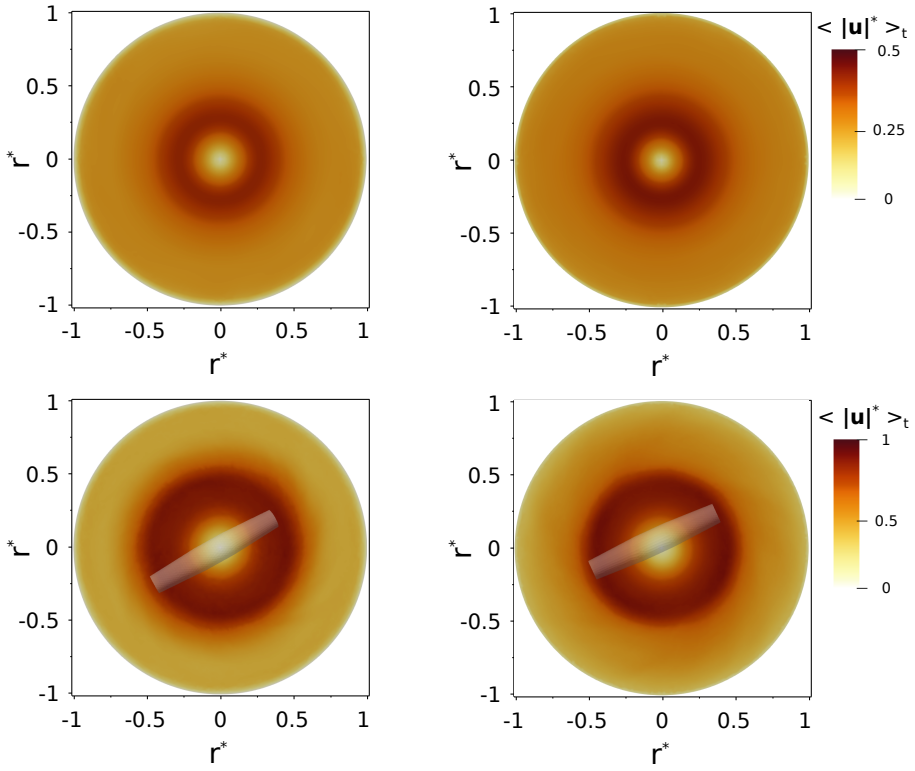

Figure 11: Time averaged flow pattern illustrated by the dimensionless velocity magnitude $< |\mathbf{u}|^* >_t$ in two horizontal planes situated respectively at $z^* = 0.03$ (bottom) and $z^* = 0.27$ (top). Left: $\mathrm{Re}_{s_1} \approx 7 \times 10^4$, right: $\mathrm{Re}_{s_2} \approx 8.6 \times 10^4$.

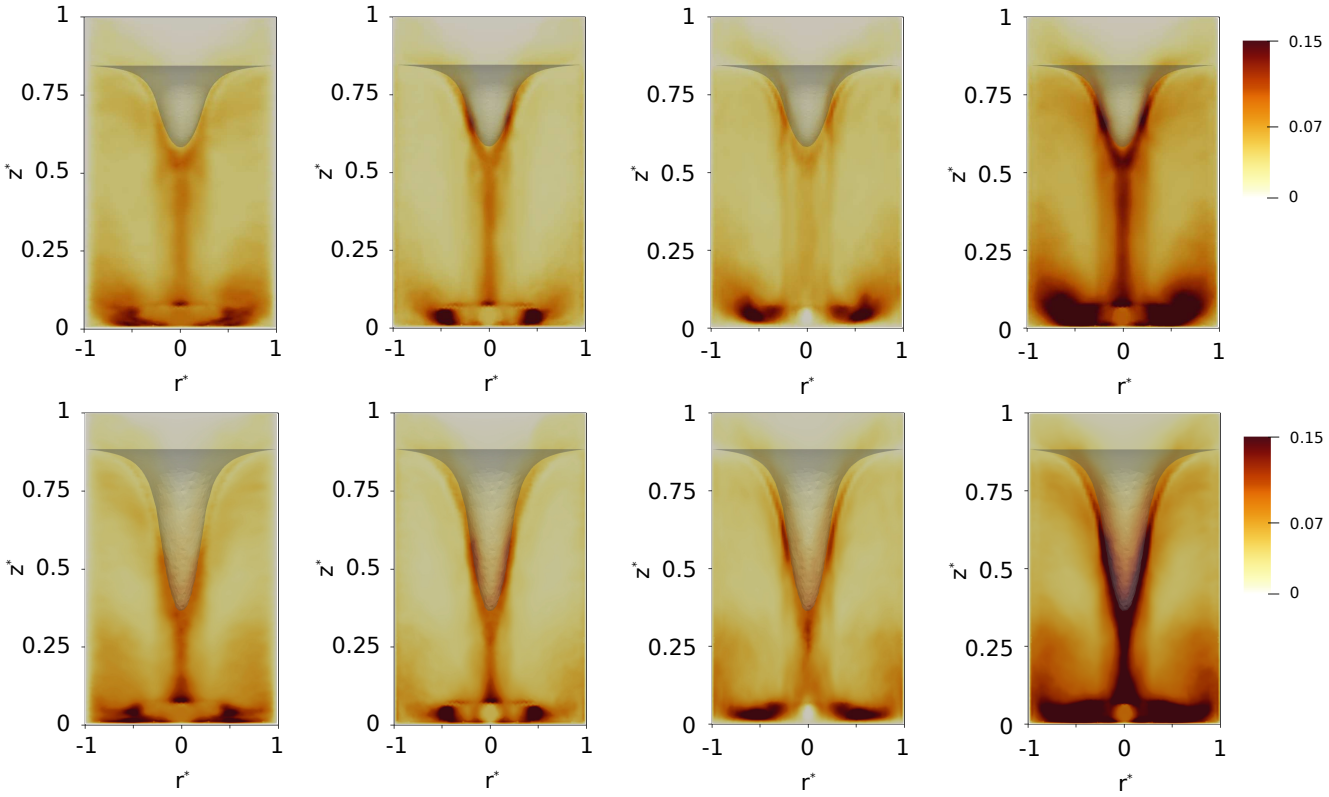

Figure 12: Velocity RMS iso-contours in the mid-vertical rz-plane. Left to right: RMS$\{u_r^*\}_t$, RMS$\{u_\theta^*\}_t$, RMS$\{u_z^*\}_t$ and RMS$\{|\mathbf{u}|^*\}_t$. Top: $\mathrm{Re}_{s_1} \approx 7 \times 10^4$, bottom: $\mathrm{Re}_{s_2} \approx 8.6 \times 10^4$.

by the mean velocity magnitude of figure 11 in two horizontal planes situated at $z^* = 0.03$ and $z^* = 0.27$.

In both cases, the tangential velocity distribution is almost uniform along z. The largest values of $< u_\theta^* >_t$ are located in the central region and near the stirrer at the bottom. They tend to zero when approaching the central axis and the walls due to the no-slip condition. A similar uniform distribution is noted on the vertical velocity component field. Negative $< u_z^* >_t$ values are situated in the central region to convect the fluid downwardly. They are positive near the wall regions to push the fluid upward, thanks to the free vortex. Besides, $< u_r^* >_t$ plays a role at the top of the RVE near the free-surface, and at the bottom at the edges of the stirrer. At the top, the fluid is pushed to the center of the vortex, while it is pushed to the walls at the bottom. Otherwise, the values of $< u_r^* >_t$ are almost negligible.

Regarding the global flow pattern, almost no influence is recorded by increasing the stirring Reynolds number. With respect to each stirring rotational frequency N, the values of the dimensionless velocity components are more or less the same. However, three main local differences are noted on the flow structure. Firstly, the variation of the free-surface vortex shape is obvious where a higher top-surface and a lower tip are obtained with $\mathrm{Re}_{s_2} \approx 8.6 \times 10^4$. Secondly, increasing the rotational velocity of the stirrer leads to different $< u_r^* >_t$ in its vicinity that is more radial in the second case. Finally, the vertical component $< u_z^* >_t$ is also affected where slight modifications are noted on the upward and downward oriented fluid zones. Qualitatively speaking, it is noted that the zone of the central forced vortex is a bit larger in the first case with $\mathrm{Re}_{s_1} \approx 7 \times 10^4$.

The velocity fluctuations are illustrated in figure 12 by the iso-contours of the root mean square (RMS) fields in the mid-vertical rz-plane situated at $\theta^* = 0$. As shown for all components, the highest oscillations are situated at the bottom of the reactor near the magnetic rod. Important but reduced values are reported in the vicinity of the forced vortex and near the top free-surface vortex. In the free vortex, the values are much smaller. As in the case of the mean fields, the RMS distribution is also symmetrical with respect to the central axis of the reactor.

5. Turbulence analysis

In this section, the auto-correlation function (ACF) and its Fourier transform are investigated to obtain information on some time frequencies associated with the flow.

5.1. Turbulent time scales

To identify the time micro-scale of Taylor λ_f, the common procedure is followed in a first approximation. For a time lag τ, the ACF is defined for a considered quantity φ at a fixed position $\mathbf{x} = (r, \theta, z)$ as

$$\mathrm{ACF}(\tau)_{\varphi(t)} = \frac{< \varphi'(t) \cdot \varphi'(t+\tau) >_t}{< \varphi'(t) \cdot \varphi'(t) >_t}, \tag{16}$$

where $\varphi'(t) = \varphi(t) - < \varphi(t) >_t$ denotes the fluctuation field.

Comparisons regarding the time-scale variation are provided for both configurations at $(r^*, z^*) = (0.09, 0.1)$ and $(r^*, z^*) = (0.8, 0.54)$. The first position corresponds to a location in the forced vortex near the stirrer, while the second is in the free region. Due to the symmetry of the flow, the following methodology is followed. For each position, eight ACF's are calculated by varying the value of $\theta^* = i/8$, where $i = \{0, 1, 2, \cdots, 7\}$. Finally, the mean ACF profile is analyzed where λ_f is identified from a good quadratic polynomial fit around the origin as stated in [26].

The mean ACF profiles are presented in figure 13 for both configurations; Re_{s_1} at the top and Re_{s_2} at the bottom. All velocity components are considered where the radial u_r is presented in red, tangential u_θ in blue and axial u_z in black. Dashed lines correspond to the fitted parabolas for which λ_f values are identified at the abscissas where the parabolas intersect the dimensionless time lag axis with $\mathrm{ACF}(\tau) = 0$. Here, τ^* is defined from the stirring frequency in the same way as the time variable (subsection 3.3).

In the forced vortex near the stirrer (figure 13, left), the correlation of u_z decreases rapidly with the dimensionless time delay τ^* in both calculations. The signature of the stirring is obviously noted on the black profiles of $\mathrm{ACF}(\tau)_{u_z}$ where a periodicity is recorded with an approximate dimensionless period between 0.5 – 0.6. Regarding the radial and tangential components, the correlation is much more important than that of u_z. A slight reduction is noted on the $\mathrm{ACF}(\tau)_{u_r}$ and $\mathrm{ACF}(\tau)_{u_\theta}$ levels by increasing the Reynolds number.

To the contrary, no periodic behavior is noted in the free vortex away from the stirrer. For both calculations, ACF profiles of all velocity components show that the correlation reduces by increasing τ^* (figure 13, bottom). It can be stated that the information is lost after two complete stirrer rotation as the ACF profiles tend to 0 at about $\tau^* \approx 2$. Like in the forced vortex case, the velocities de-correlate faster when the stirring frequency, or equivalently the Reynolds number, is increased.

The different behavior reported on the ACF, mainly in the forced vortex, implies a varying range of Taylor micro-scales. In the forced zone, the fitted parabolas of $\mathrm{ACF}(\tau)_{u_z}$ profiles state that the dimensionless value for both calculations is $\lambda_f^* = 0.12$.

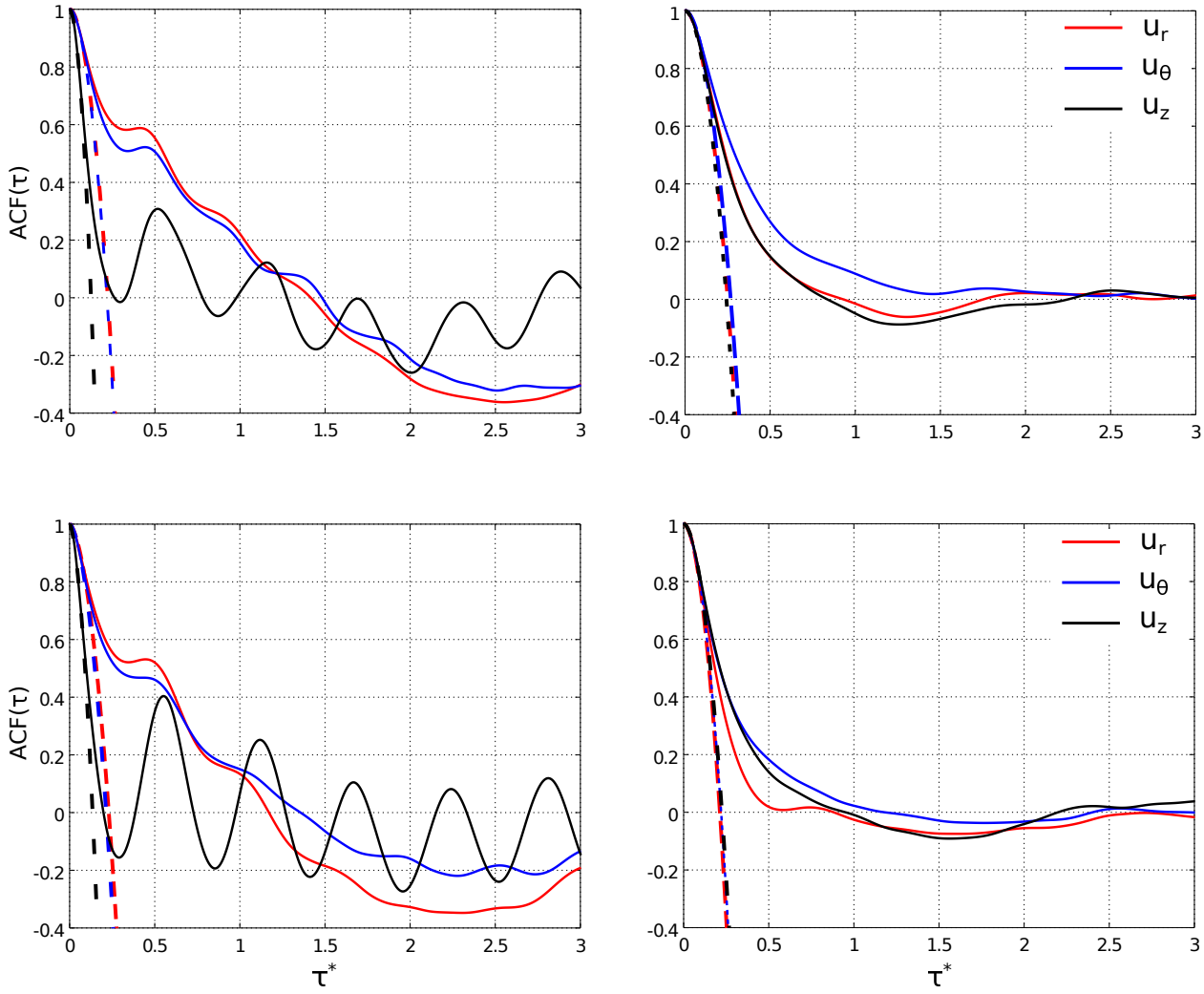

Figure 13: ACF profiles in the forced vortex (left) and in the free vortex (right). Dashed lines correspond to the fitted parabolas around the origin. Top: $\mathrm{Re}_{s_1} \approx 7{\times}10^4$, bottom: $\mathrm{Re}_{s_2} \approx 8.6 \times 10^4$.

It is much larger for components u_θ and u_r where the same micro-scale $\lambda_f^* = 0.22$ is noted in both configurations. In the free zone, the time micro-scale is almost the same for all components. It slightly decreases by increasing the Reynolds number where $\lambda_f^* = 0.25$ and 0.22 respectively for Re_{s_1} and Re_{s_2}.

5.2. *Energy spectra*

Further analysis can be provided by the energy spectra, taken as the Fourier transform of the ACF, and presented with a log-scale in figure 14. Same spatial positions are used with again the left profiles corresponding to the forced vortex near the stirrer, while the right ones refer to the free zone. The temporal spectra are also averaged over the eight symmetrical monitoring points in the $r\theta$-plane. Green solid lines are plotted on the same figure to depict the -5/3 slope, as an indication to the reader. The frequency values along the horizontal axis are normalized according to the stirring frequency. Power values along the vertical axis are normalized depending on the configuration as u_{ref}^2/N_1 or u_{ref}^2/N_2, where $u_{ref} = \{\pi N_1 D, \pi N_2 D\}$ denotes the reference velocity of each calculation.

For both calculations, the spectral analysis points out that the energy induced in the forced vortex (left figures) is much more important than that in the free zone (right figures) where the normalized power ratio can reach about 100 units as maximum and 10 as minimum. In the inertial sub-range, the power spectrum is close to the -5/3 power spectrum, commonly observed in high Reynolds number isotropic turbulence. This range is followed by the dissipation region.

A special attention is to be drawn on the spectra in the forced vortex near the stirrer. The periodicity $\tau^* = 0.5$ commented previously on the profile of $\mathrm{ACF}(\tau)_{u_z}$ is clearly observed on the spectrum of u_z'. Indeed, the peak recorded in both configurations at $f^* = 2$ justifies this observation (see figure 14, left, black profiles). It corresponds to the fact that both sides of the stirrer passes close to the position observed. At small frequencies, the energy induced by the radial and tangential velocities is more important than that induced by the axial component. A peak at a frequency $f^* \approx 0.2$ is noted in both calculations. This observation reflects a low-frequency resonance behavior that can either originate from the stirrer movement modelling and the IBM, or it may correspond to a real physical phenomenon

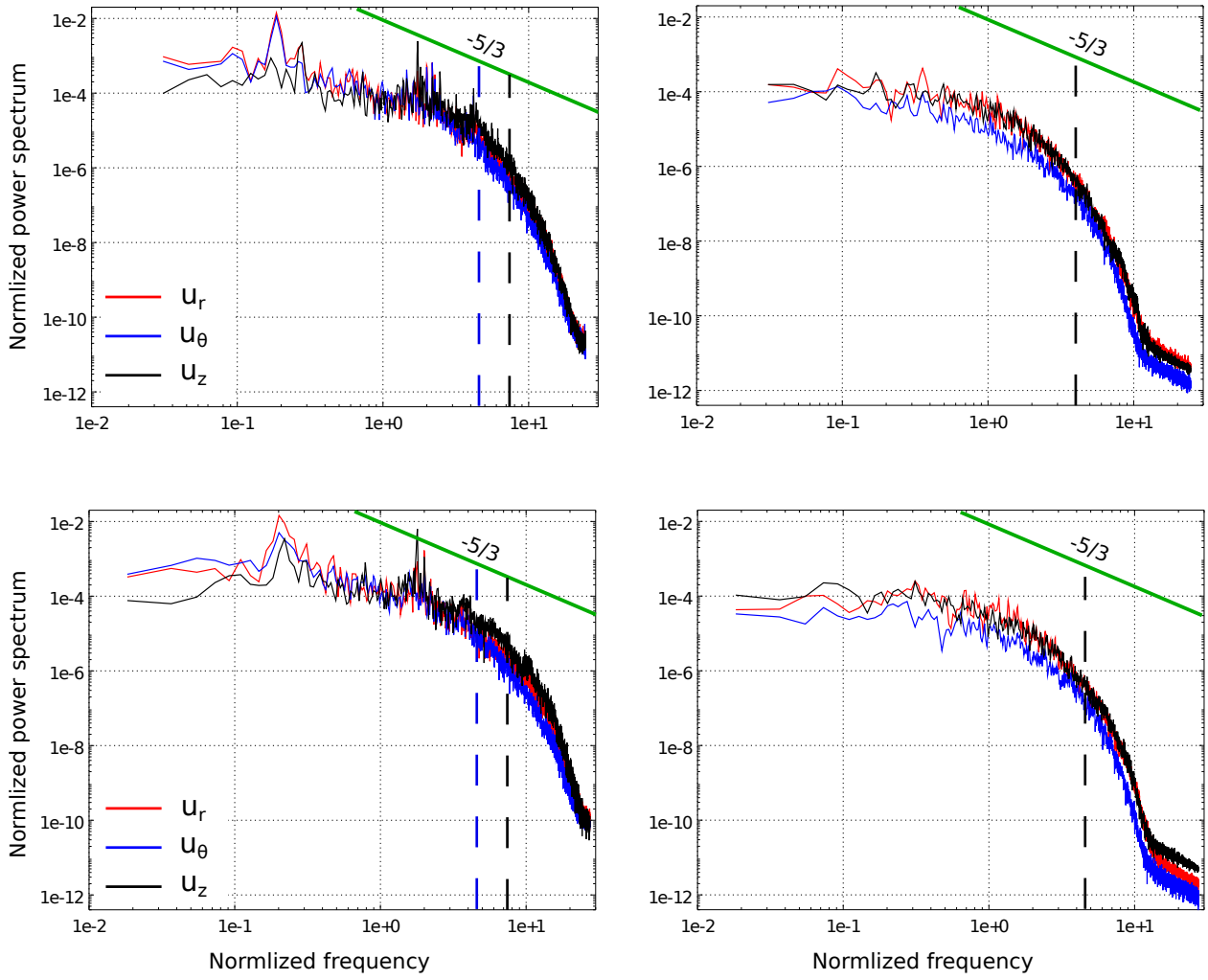

Figure 14: Energy spectra in the forced vortex (left) and in the free vortex (right). Green lines show the -5/3 slope, dashed lines depict the Taylor micro-scale frequency. Top: $\mathrm{Re}_{s_1} \approx 7 \times 10^4$, bottom: $\mathrm{Re}_{s_2} \approx 8.6 \times 10^4$.

that takes place. Further investigations are needed in a future work to understand this behavior.

The frequencies corresponding to the values of λ_f^* discussed previously are also presented in figure 14 by the vertical dashed lines. For both configurations, it is clear that the micro-scale frequency corresponding to u_z' is larger in the forced vortex due to the larger turbulence intensity that takes place in this zone, compared to the free zone. In summary, the position of these frequencies on the spectrum is coherent with the definition of these micro-scales that appear in the dissipation regime when viscous effects becomes important. Such result reflects the good quality of the performed LES, and justified the well resolved flow at the frequency of Taylor. Further investigations are required to link Taylor frequency to the stirring frequency as it may be useful to enhance mixing models.

6. Comparisons versus experimental measurements

In this section, the statistical fields are compared with the LDV measurements from the experiment carried out at CEA Grenoble. For both stirring frequencies, the time-averaged and RMS comparisons of all velocity components are provided in vertical and/or radial profiles situated in the mid-vertical rz-plane at $\theta^* = 0$. For the components u_r and u_z, the radial profiles are considered at three heights located at $z^* = 0.03, 0.28$ and 0.47 respectively. Besides, the radial profiles of the tangential velocity u_θ are considered at $z^* = 0.1, 0.28$ and 0.47. The vertical profiles are only considered for the radial and axial velocity components with $r^* = 0.6$ and 0.8.

Figure 15 (top-pairs) show the comparisons of the $< u_r >_t$ component along the three considered radial profiles. Black solid lines show the LES profiles while blue symbols denote the measured values with LDV. For both simulations, it can be clearly noted that the agreement between the LES and the LDV is very good. Indeed, the predicted/measured profiles are almost superposed, especially on highest profiles far from the stirrer. At the lowest profiles (left ones), the comparison is also satisfactory.

Similarly, the RMS$\{u_r^*\}_t$ profiles (figure 15, bottom-pairs) show a satisfactory LES/LDV agreement for both simulations. Away from the stirrer, the profiles are almost identical. At the bottom (left profiles at $z^* = 0.03$), slight variations are noted between both profiles where the predicted LES oscillations overestimates the LDV ones (maximum can reach about 20% for $\mathrm{Re}_{s_1} \approx 7 \times 10^4$ and about 30% for the second simulation with $\mathrm{Re}_{s_2} \approx 8.6 \times 10^4$). This is probably due to the sensitivity of modeling the exact motion of the magnetic stirrer, mainly for the non-dominant directions, compared to the real case.

A satisfactory agreement is also recorded along the verti-

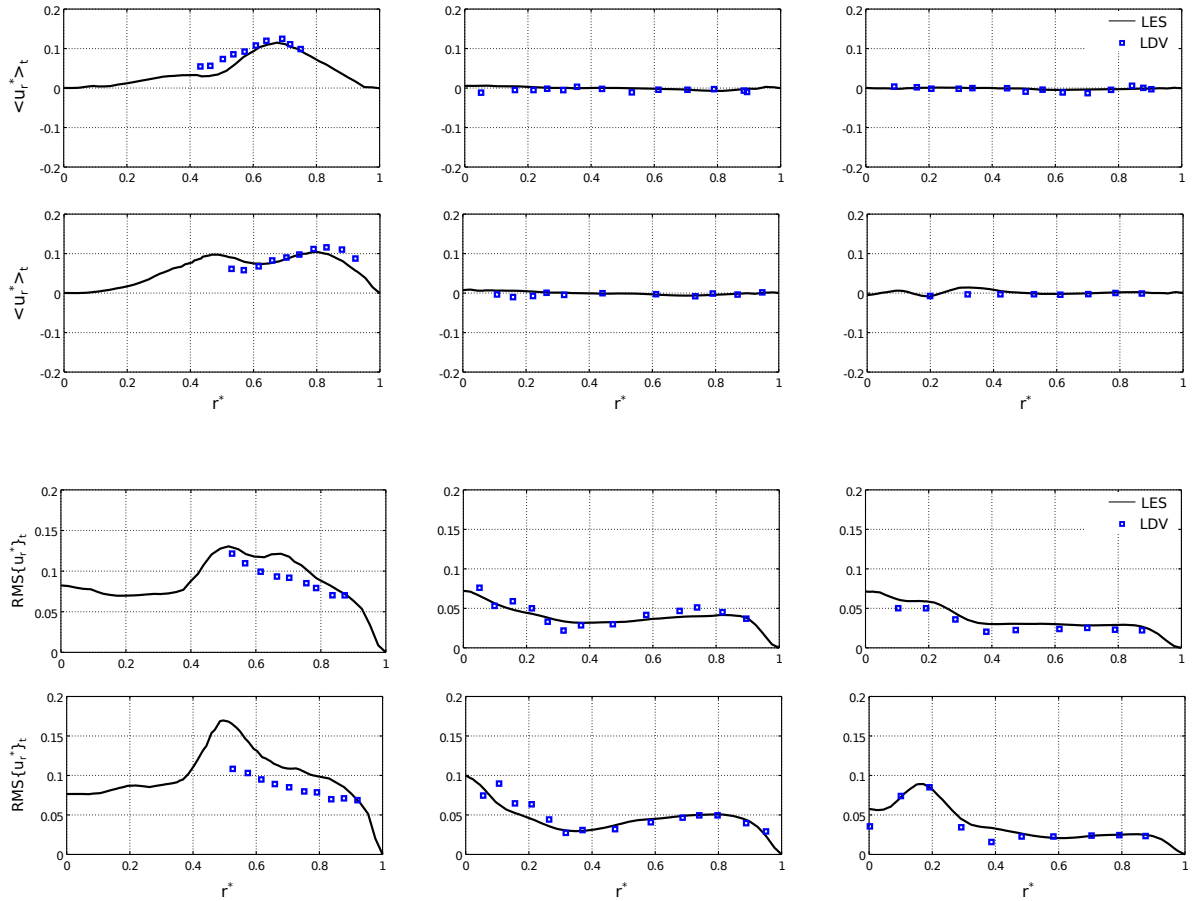

Figure 15: LES-LDV radial profiles comparisons of $< u_r^* >_t$ (top-pairs) and its RMS$\{u_r^*\}_t$ (bottom-pairs). Left to right: $z^* = 0.03, 0.28$ and 0.47 respectively. For each pair, the top profiles correspond to $\mathrm{Re}_{s_1} \approx 7 \times 10^4$, while the bottom profiles for $\mathrm{Re}_{s_2} \approx 8.6 \times 10^4$.

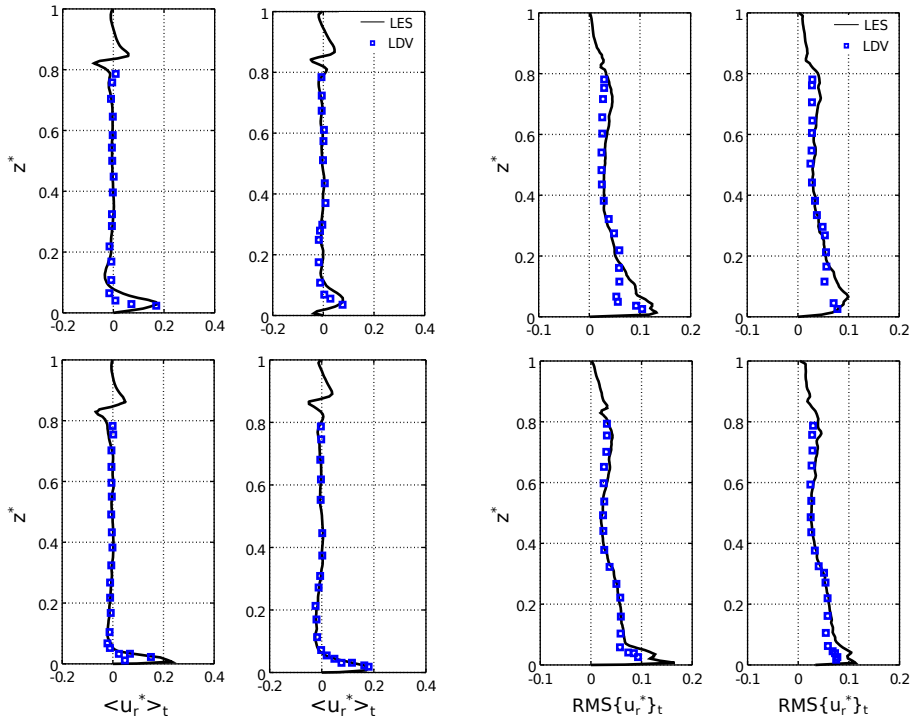

Figure 16: LES-LDV vertical profiles comparisons of $< u_r^* >_t$ (left-pairs) and its RMS$\{u_r^*\}_t$ (right-pairs). For each pair, the top profiles correspond to $\mathrm{Re}_{s_1} \approx 7\times10^4$, bottom profiles for $\mathrm{Re}_{s_2} \approx 8.6\times10^4$, left profiles for $r^* = 0.6$ while right profiles for $r^* = 0.8$.

cal profiles; both for $< u_r >_t$ and RMS$\{u_r^*\}_t$ profiles. This is illustrated in figure 16 for both calculations; top profiles are for Re_{s_1} while bottom profiles are for Re_{s_2}. For both calculations and both profiles, the predicted/measure values are almost identical. Again, slight variations are noted on the RMS values at the extremities of the stirrer which is justified by the same reason as the one stated previously.

For the dominant velocity component, the LES radial profiles of $< u_\theta^* >_t$ are in very good agreement with the measured ones (figure 17, top-pairs). For both stirring frequencies, the profiles are almost identical. Moreover, it can be stated that the influence of the stirring frequency on the dimensionless velocity is not so important as almost the same maximal values are recorded in both configurations.

Similarly for the tangential velocity fluctuations, the comparisons of the RMS$\{u_\theta^*\}_t$ profiles is very good in both cases (figure 17, bottom-pairs). Slight variations are also recorded at the lowest profile where the LES oscillations can overestimate the LDV ones by a maximum of about 20%. Again, this is a satisfactory observation and reflects the good quality of the simulations.

Finally, the LES radial profiles of u_z are compared to the measured ones in figure 18. For both simulations, the agreement of the $< u_z^* >_t$ profiles is very good (top-pairs). Slight variations are recorded on the RMS$\{u_z^*\}_t$ radial profiles, especially at the bottom near the magnetic stirrer. The same observation is also reported in figure 19 along the considered vertical profiles of $< u_z^* >_t$ and RMS$\{u_z^*\}_t$. Again as stated previously, the variations are probably originating from modelling correctly the stirrer motion. In practice, the boundary layer that forms near the stirrer is not currently taken into account, nor sufficiently resolved and it and can justify the overestimation of the velocity oscillations.

Another possible reason for the local discrepancies recorded on the RMS field might be originating from the fact that the RMS field converge slower than the mean ones. Accumulating more data might lead to a better converged RMS predictions and can reduce the recorded variations at the bottom of the tank. However, in general, it can be stated that the LES solution is globally satisfactory and is very good away from the stirrer.

7. Concluding remarks

In this paper, results from an LES of a turbulent vortex-reactor flow are presented for two stirring Reynolds numbers. The study uses the open source TRUST-TrioCFD code where a discontinuous Front Tracking algorithm is employed to detect the free surface that separates the two fluids in the reactor. An immersed boundary method is used with a penalization term to model the movement of the stirrer. A single mesh with non-uniform spatial resolution and adapted to the size of the turbulent Taylor micro-scale has been used for both cases.

The hydrodynamics is thoroughly presented and analyzed for both stirring frequencies where the expected flow pattern has been identified. In both cases, the two types of vortices that control the flow are identified in the reactor; basically the central forced vortex and the helicoidal free one. Both instantaneous and statistical flow variables are analyzed where the well known symmetrical distribution of the flow is reproduced.

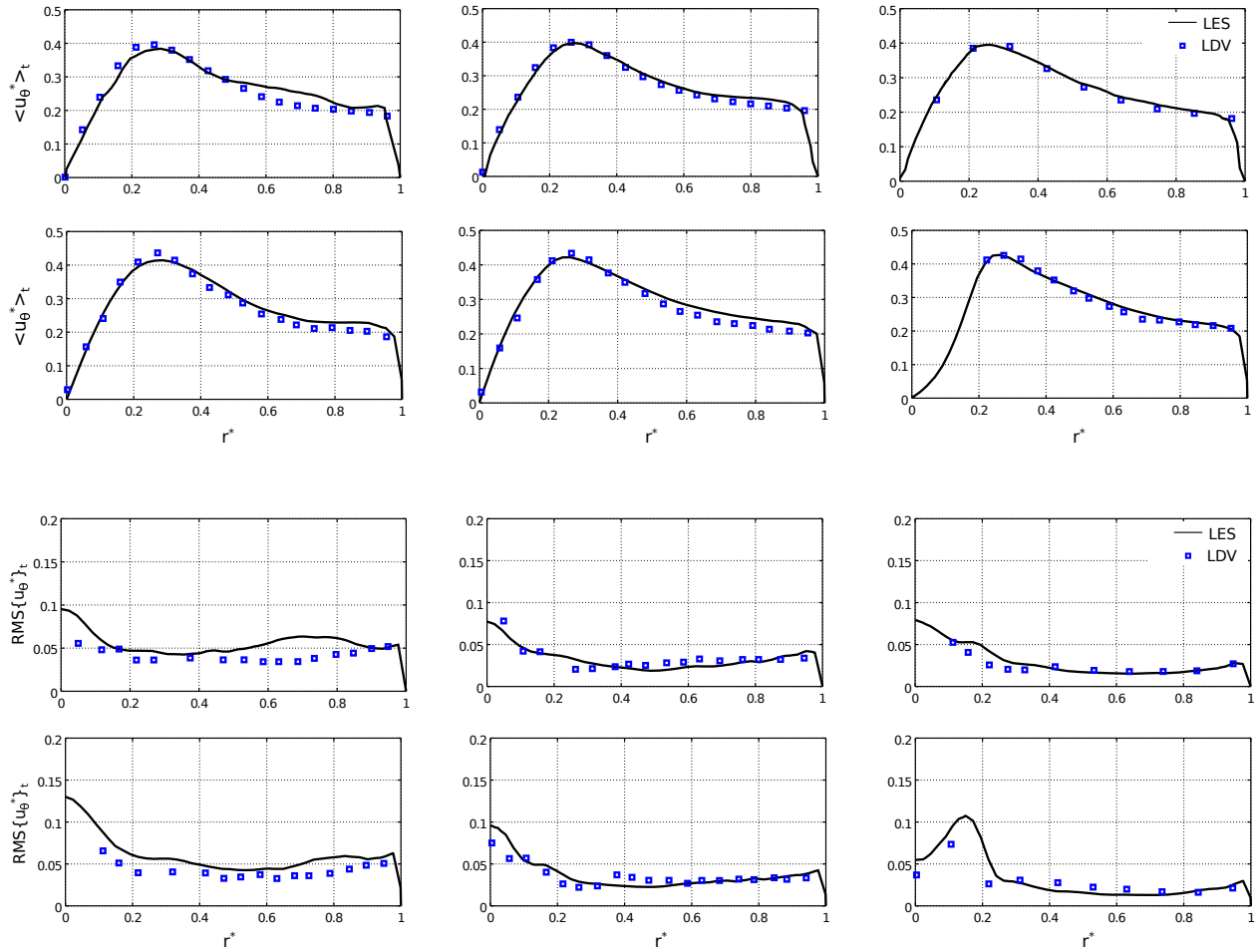

Figure 17: LES-LDV radial profiles comparisons of $< u_\theta^* >_t$ (top-pairs) and its RMS$\{u_\theta^*\}_t$ (bottom-pairs). Left to right: $z^* = 0.1, 0.28$ and 0.47 respectively. For each pair, the top profiles correspond to $\mathrm{Re}_{s_1} \approx 7 \times 10^4$, while the bottom profiles for $\mathrm{Re}_{s_2} \approx 8.6 \times 10^4$.

It has been observed that increasing the Reynolds number affects mainly the radial and vertical velocity components, but also significantly the free-surface vortex shape. No influence is reported when increasing the stirring intensity on the tangential velocity component which, in both cases, is dominant over the other components. This result is expected and is well known to take place in un-baffled stirred tanks.

The auto-correlation function and its Fourier transform are investigated in the second part of the paper. All velocity components are examined at two spatial positions depending whether the considered probe is located in the forced or in the free zone. The turbulent time micro-scales of Taylor and the periodic signature of the stirrer have been identified for both cases. It has been figured out that the Taylor micro-scales are influenced by the spatial position of the considered probe and not by the stirring frequency. This result is also important as far as the wide range of the turbulent time-scales has a significant impact on the precipitation process, the chemical saturation and the crystal formation. Analysis regarding the temporal spectra is also provided where the good quality of the performed LES is highlighted.

Finally, the LES approach is validated by comparing the numerical predictions to the LDV experimental measurements. Radial and vertical profiles are considered for all components of the velocity field at different locations. For both stirring frequencies, a very good agreement is reported on the time averaged quantities. The agreement regarding the fluctuating fields is satisfactory in general, and is very good far from the stirrer. Further investigations are to be considered in a future study in order to identify the origin of the discrepancies recorded on the oscillations near the stirrer. An improvement of the IBM approach of TrioCFD may be required to model correctly the boundary layer that develops at the stirrer edges due to its rotational movement and to the interaction with the fluid (embedded wall laws).

Acknowledgments

We acknowledge the financial support of the Cross Disciplinary Program on Numerical Simulation of CEA, the French Alternative Energies and Atomic Energy Commission. This work was granted access to the HPC resources of CINES under the allocations A0072A07571, A0062B07712 and A0082B07712 made by GENCI (Grand Equipement National de Calcul Intensif).

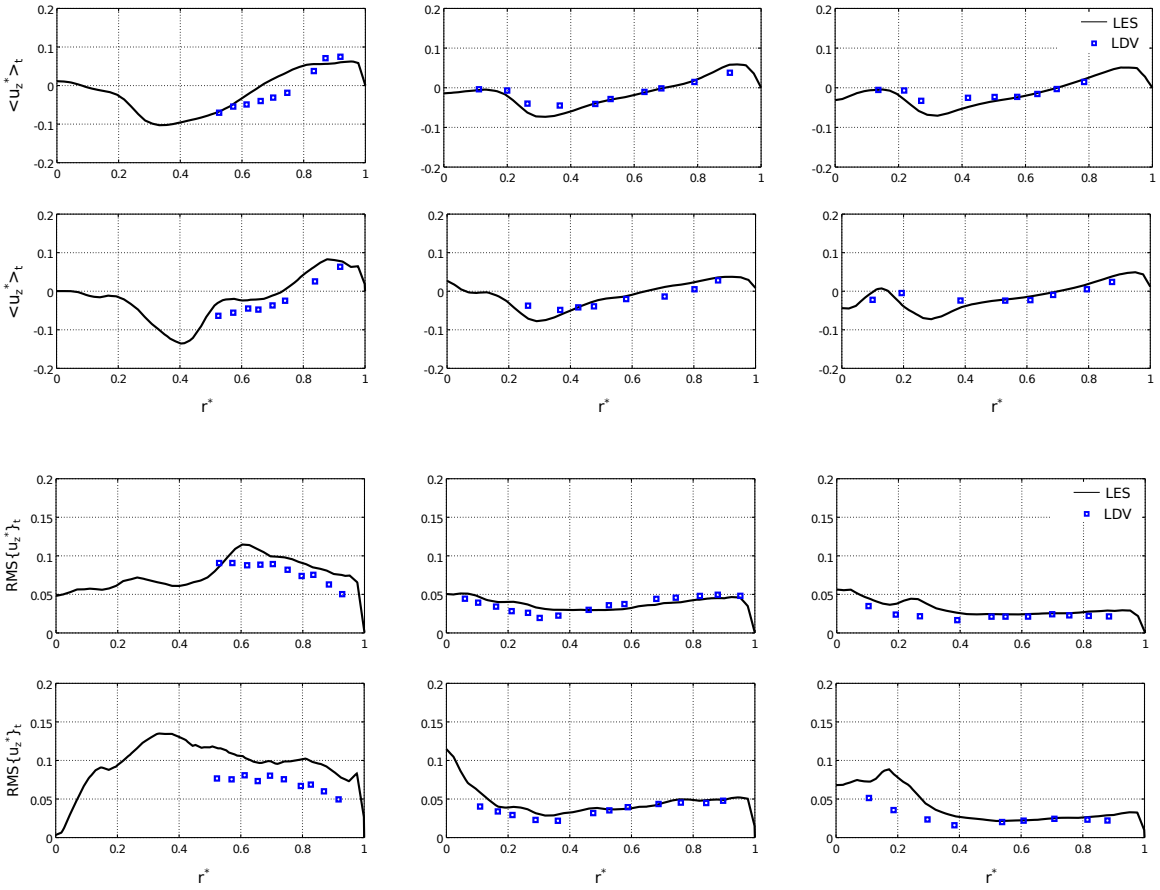

Figure 18: LES-LDV radial profiles comparisons of $< u_z^* >_t$ (top-pairs) and its RMS$\{u_z^*\}_t$ (bottom-pairs). Left to right: $z^* = 0.03, 0.28$ and 0.47 respectively. For each pair, the top profiles correspond to $\mathrm{Re}_{s_1} \approx 7 \times 10^4$, while the bottom profiles for $\mathrm{Re}_{s_2} \approx 8.6 \times 10^4$.

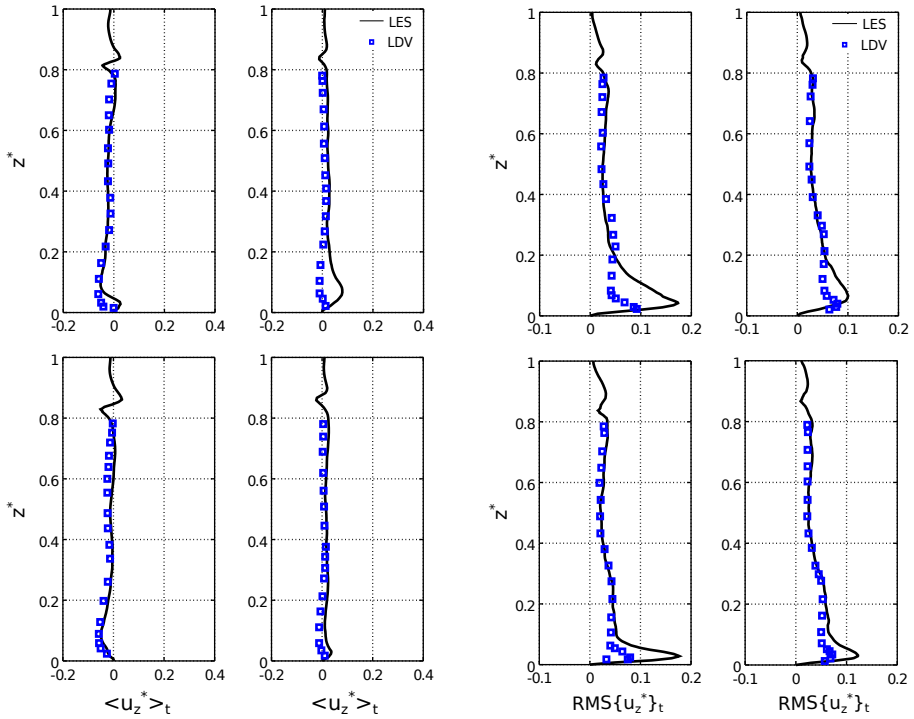

Figure 19: LES-LDV vertical profiles comparisons of $< u_z^* >_t$ (left-pairs) and its RMS$\{u_z^*\}_t$ (right-pairs). For each pair, the top profiles correspond to $\mathrm{Re}_{s_1} \approx 7 \times 10^4$, bottom profiles for $\mathrm{Re}_{s_2} \approx 8.6 \times 10^4$, left profiles for $r^* = 0.6$ while right profiles for $r^* = 0.8$.

References

[1] C Xuereb, M Poux, and J Bertrand. *Agitation et mélange: Aspects fondamentaux et applications industrielles*. Dunod, 2006.

[2] P Auchapt and A Ferlay. Appareil à effet vortex pour la fabrication d'un procédé, 1981. Brevet FR 1 556 996.

[3] DB Giaiotti and F Stel. The rankine vortex model. *University of Trieste - International Centre for Theoretical Physics*, 2006.

[4] S Nagata, N Yoshioka, and T Yokoyama. Studies on the power requirement of mixing impellers. *Memoirs of the Faculty of Engineering, Kyoto University*, 17:175–185, 1955.

[5] N Lamarque, B Zoppé, O Lebaigue, Y Dolias, M Bertrand, and F Ducros. Large-eddy simulation of the turbulent free-surface flow in an unbaffled stirred tank reactor. *Chemical Engineering Science*, 65(15):4307–4322, 2010.

[6] E Saikali, MG Rodio, G Bois, U Bieder, N Leterrier, M Bertrand, and Y Dolias. Validation of the hydrodynamics in a turbulent un-baffled stirred tank: A necessity for vortex-reactor precipitation studies. *Chemical Engineering Science*, 214:115426, 2020.

[7] M Bertrand, E Plasari, O Lebaigue, P Baron, N Lamarque, and F Ducros. Hybrid les–multizonal modelling of the uranium oxalate precipitation. *Chemical engineering science*, 77:95–104, 2012.

[8] JH Perry. Chemical engineers' handbook, 1950.

[9] E Labourasse, D Lacanette, A Toutant, P Lubin, S Vincent, O Lebaigue, JP Caltagirone, and P Sagaut. Towards large eddy simulation of isothermal two-phase flows: Governing equations and a priori tests. *International journal of multiphase flow*, 33(1):1–39, 2007.

[10] A du Cluzeau, G Bois, and A Toutant. Analysis and modelling of reynolds stresses in turbulent bubbly up-flows from direct numerical simulations. *Journal of Fluid Mechanics*, 866:132–168, 2019.

[11] G Bois. Direct numerical simulation of a turbulent bubbly flow in a vertical channel: Towards an improved second-order reynolds stress model. *Nuclear Engineering and Design*, 321:92–103, 2017.

[12] F Nicoud and F Ducros. Subgrid-scale stress modelling based on the square of the velocity gradient tensor. *Flow, turbulence and Combustion*, 62(3):183–200, 1999.

[13] J Smagorinsky. General circulation experiments with the primitive equations: I. the basic experiment. *Monthly weather review*, 91(3):99–164, 1963.

[14] U Schumann. Subgrid scale model for finite difference simulations of turbulent flows in plane channels and annuli. *Journal of computational physics*, 18(4):376–404, 1975.

[15] Christophe Calvin, Olga Cueto, and Philippe Emonot. An object-oriented approach to the design of fluid mechanics software. *ESAIM: Mathematical Modelling and Numerical Analysis*, 36(5):907–921, 2002.

[16] DES-CEA. TrioCFD, http://triocfd.cea.fr/.

[17] T Fortin. *Une méthode d'éléments finis à décomposition L2 d'ordre élevé motivée par la simulation des écoulements diphasiques bas Mach*. PhD thesis, Université Paris 6, 2006.

[18] PE Angeli, U Bieder, and G Fauchet. Overview of the trio cfd code: main features, v&v procedures and typical applications to nuclear engineering.

[19] E Saikali. *Numerical modelling of an air-helium buoyant jet in a two vented enclosure*. PhD thesis, Sorbonne Université, 2018.

[20] E Saikali, G Bernard-Michel, A Sergent, C Tenaud, and R Salem. Highly resolved large eddy simulations of a binary mixture flow in a cavity with two vents: Influence of the computational domain. *International Journal of Hydrogen Energy*, 44(17):8856–8873, 2019.

[21] EA Fadlun, R Verzicco, Paolo Orlandi, and J Mohd-Yusof. Combined immersed-boundary finite-difference methods for three-dimensional complex flow simulations. *Journal of computational physics*, 161(1):35–60, 2000.

[22] M Belliard, M Chandesris, J Dumas, Y Gorsse, D Jamet, C Josserand, and B Mathieu. An analysis and an affordable regularization technique for the spurious force oscillations in the context of direct-forcing immersed boundary methods. *Computers & Mathematics with applications*, 71(5):1089–1113, 2016.

[23] B Mathieu. A 3d parallel implementation of the front-tracking method for two-phase flows and moving bodies. *177ème Session du comité scientifique et technique de la Société Hydrotechnique de France, Advances in the modelling methodologies of two-phase flows, Lyon, France*, 2004.

[24] A Du Cluzeau, G Bois, A Toutant, and JM Martinez. On bubble forces in turbulent channel flows from direct numerical simulations. *Journal of Fluid Mechanics*, 882:A27, 2020.

[25] platform V9.7.0 SALOME. https://www.salome-platform.org/news.

[26] SB Pope. Turbulent flows, 2001.

[27] H Reichardt. Vollständige darstellung der turbulenten geschwindigkeitsverteilung in glatten leitungen. *ZAMM-Journal of Applied Mathematics and Mechanics/Zeitschrift für Angewandte Mathematik und Mechanik*, 31(7):208–219, 1951.

[28] U Bieder and C Genrault. Cfd analysis of intra and inter fuel assembly mixing. *Annals of Nuclear Energy*, 135:106977, 2020.

[29] U Bieder, H Uitslag-Doolaard, and B Mikuž. Investigation of pressure loss and velocity distribution in fuel assemblies with wire-wrapped rods by using rans and les with wall functions. *Annals of Nuclear Energy*, 152:108025, 2021.

[30] OCCIGEN-CINES. https://www.cines.fr/calcul/materiels/occigen.

[31] E Saikali, G Bois, MG Rodio, U Bieder, M Bertrand, N Leterrier, and Y Dolias. Influence of the hydrodynamics and the reaction-rate formulation in modeling infinitely fast irreversible reactions in a turbulent unbaffled chemical reactor. *Chemical Engineering Communications*, pages 1–31, 2020.